Uniform Huygens Metasurfaces with Postfabrication Phase Pattern Recording Functionality

Elena Mikheeva, Remi Colom, Patrice Genevet, Frederic Bedu, Igor Ozerov, Samira Khadir, Guillaume Baffou, Redha Abdeddaim, Stefan Enoch, Julien Lumeau

Uniform Huygens metasurfaces spectral tuning as a mass-production perspective

Elena Mikheeva,[†,‡] Remi Colom,[†] Patrice Genevet,[*,†] Frederic Bedu,[¶] Igor Ozerov,[¶] Samira Khadir,[†] Guillaume Baffou,[§] Redha Abdeddaim,[§,‖] Stefan Enoch,[§,‖] and Julien Lumeau[*,§,‖]

†*Université Côte d'Azur, CNRS, CRHEA, Rue Bernard Gregory, Sophia Antipolis 06560 Valbonne, France*

‡*Multiwave Innovation SAS, 2 Marc Donadille, 13453 Marseille, France*

¶*Aix Marseille Univ, CNRS, CINAM, 13009 Marseille, France*

§*Aix Marseille Univ, CNRS, Centrale Marseille, Institut Fresnel, F-13013 Marseille, France*

‖*These authors contributed equally to this work*

E-mail: patrice.genevet@crhea.cnrs.fr; julien.lumeau@fresnel.fr

Abstract

With the rapid progress in the field of metasurfaces and their use in miniature integrated devices arise the quest for cheap mass production of efficient metasurfaces. We suggest a novel way to design and fabricate phase-gradient Huygens metasurfaces using laser-annealing of uniform particles made of As_2S_3 chalcogenide glass. We show that a phase gradient metasurface can be realized by tuning the refractive index of otherwise identical meta-atoms instead of tuning their geometry. We are using an array of identical As_2S_3 particles with the possibility to locally change their refractive index using a short-wavelength illumination (green laser) in order to tune the phase

pattern at the post-fabrication stage. Metasurfaces fabricated with this method can be used for operation in the red or IR spectral range. We fabricate uniform As_2S_3 Huygens metasurfaces using electron beam lithography and demonstrate their post-fabrication tuning with exposure of comparatively low intensity. Samples characterization with transmittance measurement and quantitative phase microscopy provide results in good correspondence with numerical predictions confirming post-fabrication spectral tuning. Using such tuning, we demonstrate the possibility to transfer the intensity pattern produced by modifying a writing beam with a spatial light modulator to a phase pattern recorded on a uniform As_2S_3 metasurface. Our method has potential advantages for the low-cost production of large-scale metasurfaces because uniform geometries are better adjusted for mass manufacturing.

Introduction

Metasurfaces are nano-structured ultra-thin miniature optical components, typically a few hundred nanometers thick, that provide arbitrary light control capabilities.[1,2] Research on metasurfaces bursted during the last decade, providing various implementations and inspiring promising applications ranging from laser wavefront engineering to compact LiDARs.[3–6]

In particular, wavefront shaping, being one of the most promising directions of metasurfaces application, requires the device to locally introduce a full 2π phase gradient to the incident field. There are several principal physical mechanisms for that, such as (i) using the propagation phase control through non-resonant nanopillars with varying filling factor,[7–11] (ii) using geometric phase accumulation controlled by the orientation of anisotropic scatterers,[12–14] and (iii) using the scattering phase produced by resonant pillars.[15–18] For active modulation of metasurfaces with fixed structural parameters, using resonant phase from relatively high quality factor resonances appears to be a unique solution to achieve a full phase tuning, especially using tunable material with a relatively small refractive index change.

It has recently been proposed theoretically that a full 2π resonant phase gradient can

be produced in metasurfaces by breaking symmetries.[19] Parity-time breaking in reflection or time-reversal symmetry breaking in transmission are shown to relax the restrictions on the values of system eigenfrequencies of different types. In particular, reflection and transmission zeros in the structures with broken symmetries are allowed to move in a complex plane which could lead to a pair of eigenvalues (pole and zero, eigenvalues calculated with different boundary conditions) being separated by the real frequency axis. This is now clearly understood as the necessary condition to achieve full 2π phase accumulation as a function of the real frequency. Considering the low-loss dielectric materials we selected for the design, we choose to work in transmission which guarantees higher components efficiency by avoiding potentially lossy mirrors. In transmission, explicit time-reversal symmetry breaking requires gain-loss engineering which is not technologically relevant to this problem. The other solution is spontaneous symmetry breaking which relies on the interaction of two zeros associated with two resonant modes, the effect demonstrated in Huygens metasurfaces.[19] Therefore, in transmission, our choice is limited to Huygens metasurfaces that have been, and still are, receiving tremendous attention due to their ability to reach high efficiencies combined with a full 2π phase coverage for arbitrary wavefront shaping.[15] The expertise in designing and fabricating Huygens metasurfaces with different materials and realizing them using various fabrication techniques, has enabled an impressive amount of optical components and devices.[16,20–35]

Huygens metasurfaces can be implemented as fixed-functionality components with a unique phase pattern created by geometric parameters variation (resonators size or period)[15,16,20–24,26,29,30] or as actively tunable devices with uniform unit cells activated by applying external stimuli.[33–35] In this paper, we are suggesting an intermediate option of using the material's fine-tuning for the fabrication of passive (fixed-functionality) metasurfaces with uniform-sized unit cells. In other words, phase patterns would be recorded on the uniform grids using local refractive index change in metasurface unit cells. For this purpose, we suggest As_2S_3 chalcogenide glass well-known for waveguides and fibers manufacturing and

for the micrometer-scale optical components.[36] After fabrication, this material experiences refractive index change resulting from transferring to the material above-bandgap energy in different ways, such as thermal exposure, exposure by an electron beam, illumination by the radiation from ultra-violet[37] to visible green light,[36] etc. It was shown, that exposure to the light of small fluence allows changing the refractive index while preserving the surface structure and keeping the height of the exposed material constant.[38,39] Therefore, we suggest fabricating uniform As_2S_3 Huygens metasurfaces and tuning them with the green or blue light for operation in red on IR frequency ranges.

In this work, we design high-efficiency Huygens metasurfaces made of As_2S_3 chalcogenide glass, fabricate them by electron-beam lithography, and characterize them with several techniques: with the conventional spectroscopic transmittance measurement, and a phase microscopy technique performed in a broad wavelength range. We also demonstrate uniform Huygens metasurfaces post-fabrication tuning by recording a binary phase pattern using intensity-modulated light exposure at 532 nm. The tuned metasurface produced a hologram in the far field while being illuminated at its operation wavelength 940 nm. This experiment confirms the possibility of transferring the on-demand phase pattern to a uniform fine-tunable metasurface using a spatial light modulator.

Results and discussion

Design and theoretical description of Huygens metasurfaces

We numerically design a Huygens metasurface composed of resonant As_2S_3 particles arranged into a 2D square zero-order diffraction grating patterned on an infinite glass substrate. We considered nanoparticles made of a lossless material, and to further maximize the component's transmission efficiency, we surround the nanostructures with a transparent embedding medium ($n_{med} = n_{sub} = 1.5$) as shown in Fig. 1a. We fix the unit cell period at $p = 450$ nm, the particle height at $h = 195$ nm, and the particle side length L is left as a varying param-

eter to explore different operation regimes. The refractive index of As_2S_3 in the initial state (right after the deposition) is $n \approx 2.41$ at the wavelength $\lambda \approx 800\ nm$ ($f \approx 375\ THz$).

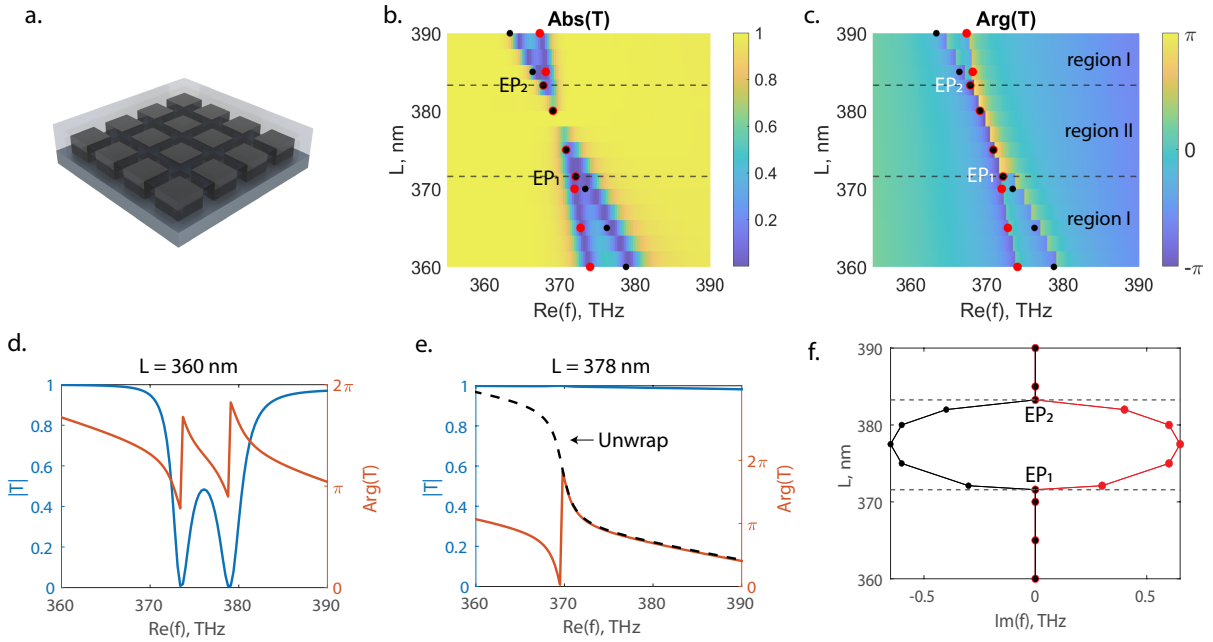

Figure 1: a. Schematic representation of a metasurface composed of a 2D square lattice of rectangular As_2S_3 particles. The substrate and the embedding medium are both chosen to have the same refractive index $n = 1.5$. b. and c. present the transmission spectrum (respectively the amplitude and the phase) of the metasurface shown in (a) as a function of the particle size L. Red and black points show the trajectories of the real parts of the two complex transmission zeros f_{z1}, f_{z2}. d. Transmission amplitude and phase as a function of frequency for the region (i): two spectrally separated transmission zeros each providing a π phase jump. e. Transmission amplitude and phase as a function of frequency for the region (ii): high transmission caused by transmission zeros expelled into the complex plane. Phase here experiences a 2π jump (red line) which, after applying phase unwrap, turns into a smooth 2π phase variation (black dashed line) f. Trajectories of the imaginary parts of the two complex zeros f_{z1}, f_{z2} as a function of the particle size L. Trajectories of zeros real and imaginary parts in c. and d. reveal that the Huygens regime providing high transmission amplitude and 2π phase variation is bounded by the two transmission zeros Exceptional Points EP_1 and EP_2.

Numerical results have been obtained by considering a plane wave excitation impinging on the device at normal incidence. The transmission coefficient calculated as a function of the real part of the excitation frequency and the particle size ranging from $L = 360\ nm$ to $L = 390\ nm$, was obtained using commercial software CST Studio Suite. The amplitude of

calculated transmission spectra shows 2 transmission minima, or transmission zeros, that are getting closer and closer to each other to finally disappear in a range of L values ranging from $\approx 371.58\ nm$ to $\approx 383.26\ nm$. In the vicinity of the overlapping region, the transmission is significantly enhanced (Fig. 1b). Looking at the phase response as a function of L in ((Fig. 1c), we observed different operating regimes: (i) the position of each transmission minima are spectrally separated, each associated with a π transmission phase jump, (ii) the phase discontinuity of the transmission coefficient provides a 2π transmission phase jump of interest for a full wavefront phase modulation.

We have demonstrated in our previous work that Huygens metasurfaces behavior is governed by the positions in the complex frequency plane of topological phase singularities (zeros and poles of the transmission coefficient) - special points in the complex frequency plane that are turning metasurface optical transmission into zero or infinity, respectively, with the phase value wrapping around the singular point.[19] These two types of singularities have the opposite topological charge ± 1, they exist in pairs of the opposite charge and can annihilate when they superimpose. Zeros and poles are generally complex-valued. This originates from the non-Hermitian nature of the metasurface caused by the existence of either absorption losses in the metasurface material or by scattering losses. According to the Weierstrass factorization fundamental theorem in the field of complex analysis, any rational function of a complex variable can be represented with the equation (1) containing an infinite number of poles f_p and zeros f_z in the complex frequency plane:[40–47]

$$T(\omega) \propto \prod_{n=-\infty}^{\infty} \frac{f - f_{\mathrm{z},n}}{f - f_{\mathrm{p},n}}, \tag{1}$$

In the following, we consider the transmission coefficient in a frequency region that is dominated by only 2 zero-pole pairs denoted respectively as f_{z1}, f_{p1}, and f_{z2}, f_{p2}. Consequently, taking into account only the two terms associated with these two pairs in Eq. 1 provides already a good qualitative prediction of the transmission coefficient in the region of interest. The transition in the behavior of the transmission coefficient can mostly be under-

stood by studying the trajectories of zeros just as in.[19] Therefore, we calculate the designed metasurface response (Fig. 1a) with JCMwave software (see Materials and Methods section) using complex frequency excitation and extract complex zeros positions f_{z1} and f_{z2}. We show their trajectories as functions of particle size L in Fig. 1b,c ($Re(f_{z1})$ and $Re(f_{z2})$) and in Fig. 1f ($Im(f_{z1})$ and $Im(f_{z2})$). While the real parts of zeros trace the trajectory of transmission dips, imaginary parts show two distinct operation regimes (i) and (ii) characterized by real-valued and complex zeros respectively. Regime (ii) is known in the literature as the Huygens metasurface regime. At the boundaries between the two operation regimes, the zeros overlap completely ($f_{z1} = f_{z2}$) forming exceptional points on the real axis (EP_1 and EP_2). We calculate the positions of the EPs: $f_{EP_1} \approx 372.1\ THz$ at $L_{EP_1} = 371.55\ nm$ and $f_{EP_2} \approx 367.8\ THz$ at $L_{EP_2} = 383.26\ nm$. We discuss in more detail zeros trajectories around the exceptional point in the Supplementary Information.

When a full 2π phase gradient is required, Huygens metasurface should be operating in the parameter region where the two zeros are moved to the complex frequency plane with complex conjugated frequencies. This region is separated by the transmissionless EPs (see SI for more information). In the following section, we will fabricate and characterize As_2S_3 Huygens metasurfaces.

As_2S_3 metasurfaces fabrication and spectral tuning

As_2S_3 is a photosensitive material, which is characterized by changes in the refractive index and the extinction coefficient upon illumination by light with an energy above the material bandgap ($\approx> 2eV$). For reference, the As_2S_3 material properties after deposition and prior illumination are shown in Fig. 2a. The metasurface we designed is operating at the near-IR wavelength (in the vicinity of $\lambda = 800\ nm$), to make use of a green light at $\lambda = 532\ nm$ for fine-tuning of the metasurface response at near-IR. Preliminary measurements of the refractive index change at $\lambda = 800\ nm$ depending on the incident green light fluence is shown in Fig. 2b.[38]

Then metasurface samples were produced using the following procedure. First, As_2S_3 layer was fabricated with the electron-beam vapor deposition technique, its thickness was characterized with the transmission measurement ($h = 195\ nm$). Afterward, samples were nanostructured with electron-beam lithography and etched by inductively coupled argon plasma. Several metasurfaces were fabricated with electron-beam patterns with a different pitch between the particles and with different electron-beam exposure doses (from 40 to 48 $\mu C/cm^2$) which resulted in metasurface samples with different particle sizes L (Fig. 2c). Finally, the structure was covered by spin-coating with a thin layer of Poly(methyl methacrylate) (PMMA) polymer acting as the embedding medium ($n \approx 1.48$). The fabrication process leads to the partial refractive index change due to the e-beam exposure and thermal heating at the stage of resist conditioning on a hotplate. After this process, the partially-exposed fabricated metasurface has a refractive index marked with "1" in Fig. 2b. It is possible to further change the fabricated sample refractive index to the value marked with "2" (Fig. 2b.). These two refractive index points are considered the initial and the final index for the performed transmission amplitude and phase measurements. The fabrication process is described in more detail in the Methods section.

Transmission spectra for selected samples were measured before and after green laser exposure (refractive indices before and after this exposure correspond to the points 1 and 2 in Fig. 2b.), measurement technique described in the Methods section. Measurement results (Fig. 2d) show a significant red shift between spectra of the initial and light-annealed structures (T_1 and T_2). We first observe that transmission spectra before and after annealing present two transmission minima that are approaching each other as the particles size increases. These results are compared to the simulation done in CST Studio (r) with $p = 450\ nm$, $h = 195\ nm$, $n_{sub} = 1.5$, $n_{med} = 1.48$, the size of the particles L correspond to the sizes measured from SEM images (Fig. 2c). To take into account fabrication uncertainty, including local change of the particle size within the same array, each simulation result was averaged over 11 values varying from $L - 5\ nm$ to $L + 5\ nm$. Results shown in Fig. 2e

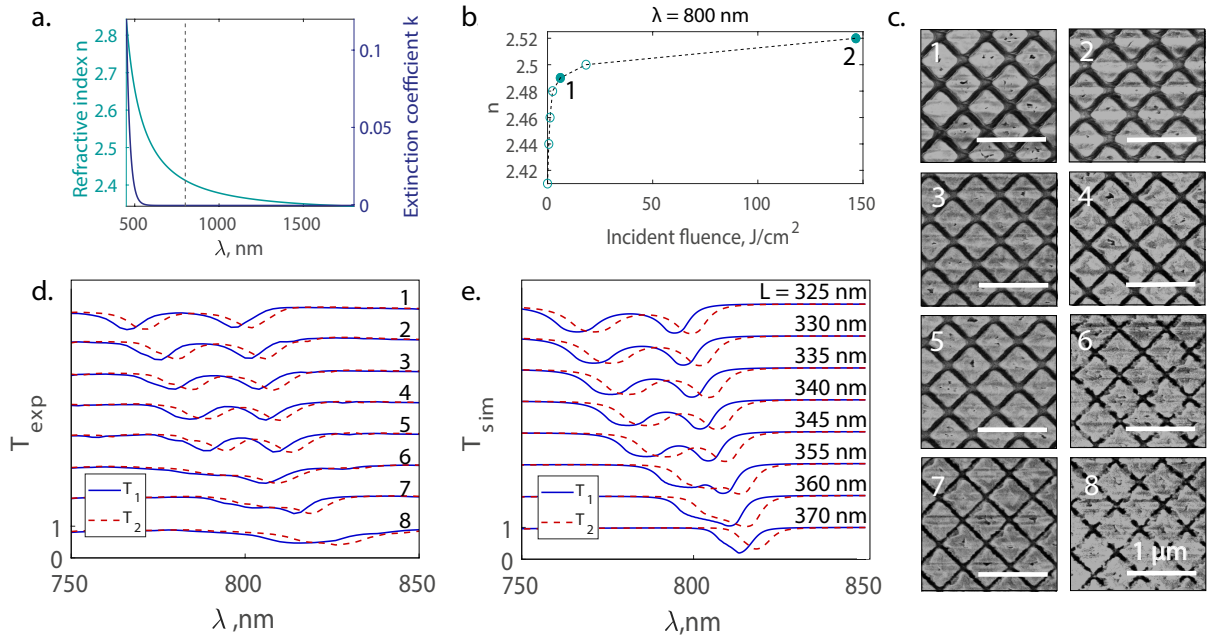

Figure 2: a. Complex refractive index of As_2S_3 measured immediately after deposition and before illumination with the green tuning light. b. Refractive index change at $\lambda = 800\ nm$ as a function of fluence of incident green light ($\lambda = 532\ nm$). c. SEM images of fabricated metasurface samples of various size L d. Experimental transmission spectra measured for the samples shown in (c) before (T_1 in blue full line) and after light-annealing (T_2 in red dashed lines) and e. corresponding numerical transmission spectra simulated for different average size L (results from $L - 5\ nm$ to $L + 5\ nm$ were calculated with a step 1 nm and averaged) before (T_1) and after (T_2) light-annealing.

are in good correspondence with the experimental data. These results correspond to the operation regime away from the Huygens response (Fig. 1b.,c.) below the exceptional point EP_1, approaching the EP_1 for the larger value of particles size L.

As a next step, we image the phase distribution of the transmitted light produced by several selected samples using quadriwave lateral shearing interferometry (QLSI, see Methods section for more detail).[48,49] To illustrate the method, we show an example of a measurement performed with this technique on one of the fabricated metasurfaces (sample 3 on the Fig.2c), measurement was done at $\lambda = 765\ nm$. First, we measure the phase profile of the transmitted light without laser illumination, as a reference, then turn on a blue laser (OBIS 488 from Coherent) focused on a $\approx 25\ \mu m$ spot on a sample and expose ensuring maximum exposure dosage from the Fig. 2b in order to locally trigger photosensitivity of the As_2S_3 material.

As shown on the measured intensity and phase maps (Fig. 3a,d) we clearly see the contrast between the exposed and non-exposed areas of a metasurface.

Results of the transmission amplitude and phase measurement with the QLSI for 2 selected samples (sample 4 and 7 in figure Fig. 2c) before and after exposure are shown in Fig. 3b (transmittance amplitude), and in Fig. 3e (transmittance phase). These results are in good agreement with the simulations performed in CST Studio (r) and averaged over 11 values varying from $L - 5nm$ to $L + 5nm$ to consider fabrication uncertainty of ± 5 nm (Fig. 3c,f). We note that these measurements still correspond to the operation regime slightly outside of the Huygens regime(Fig. 1b.,c.). However, the measurement for the sample with $L = 360$ nm is in very close proximity to the first exceptional point EP_1, and the unconventional shape of the phase curve is due to averaging of sizes that provide 2π resonant phase jump and sizes that provide two closely located but separated π jumps.

We would like to point out that reaching the Huygens regime in As_2S_3 metasurfaces at this operation wavelength (≈ 800 nm) requires fabrication techniques capable of producing small gaps between nanoparticles (below 70 nm) with more than 2.5 aspect ratio. These dimensions turned out to be challenging for the current fabrication technique. However, this design can be used at longer operation wavelengths considering its comparatively high refractive index and transparency in a large wavelength region (Fig. 2a). Scaling this structure up would increase the size of the smallest fabrication features.

Post-fabrication phase pattern recording

The developed method combining standard fabrication of uniform metasurfaces and their tuning with light exposure has the potential for mass manufacturing of phase-gradient metasurfaces, as explained in our recent patent.[50] Here, we produce a demonstration of a binary optical hologram using a spatial light modulator for the partial exposure of the photosensitive sample. As we are trying to reach the Huygens regime for higher phase contrast between exposed and unexposed parts of the metasurface, it is scaled up to operate at ≈ 940 nm. The

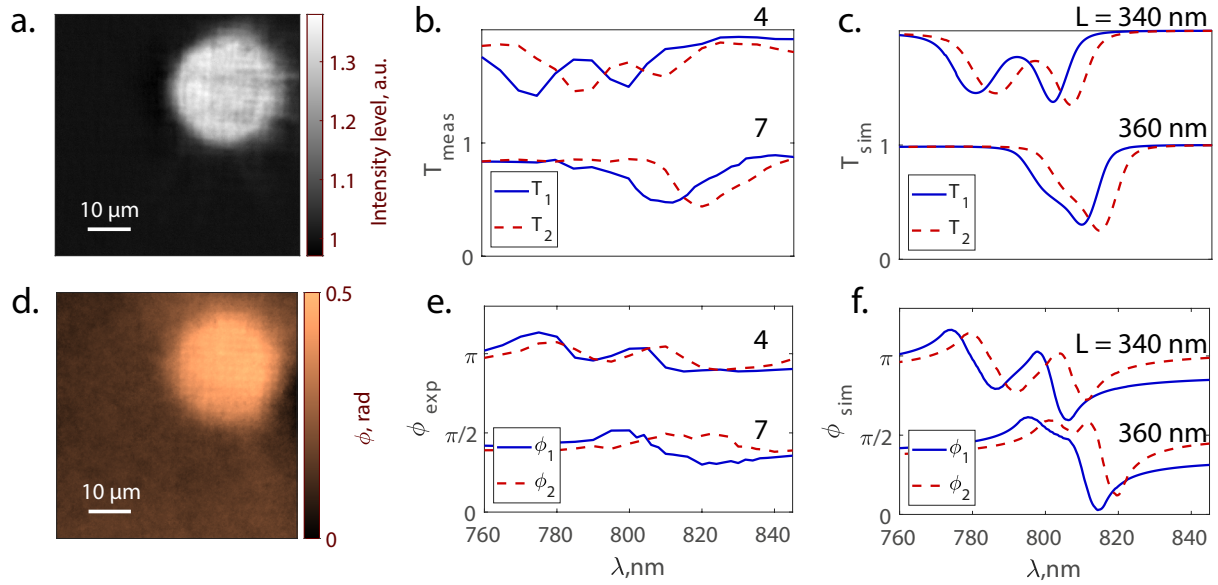

Figure 3: a. Intensity and d. Phase images showing the transmittance through the non-exposed metasurface compared to the spot annealed with the focused laser b. Transmittance amplitude measurement of samples 4 and 7 in 2(a) before (T_1) and after (T_2) blue laser exposure. c. Transmittance amplitude simulation for $L = 340 \pm 5\ nm$ and $L = 360 \pm 5\ nm$ before(T_1) and after (T_2) light annealing. e. Transmittance phase measurement of the samples 4 and 7 in 2(a) before (ϕ_1) and after (ϕ_2) blue laser exposure. f. Transmittance phase simulation for $L = 340 \pm 5\ nm$ and $L = 360 \pm 5\ nm$ before(ϕ_1) and after (ϕ_2) light annealing.

As_2S_3 metasurface working in the vicinity of this wavelength has period $p = 540\ nm$, height $h = 220\ nm$, refractive index $n \approx 2.39$, and it is embedded in PMMA with $n_{PMMA} \approx 1.48$. Simulation of the transmission phase through this metasurface shown in Fig. 4a. predicts the Huygens regime for resonators sizes $\approx 440 - 460\ nm$. This metasurface of size $1 \times 1\ mm$ was fabricated with the same method (please refer to Methods section). The thickness of the fabricated As_2S_3 film was measured using optical monitoring throughout the deposition ($h \approx 220 \pm 10\ nm$), the dimensions of the fabricated structure were measured using SEM-images (Fig.4b.), the period $p \approx 540 \pm 10\ nm$, the sizes $L = 450 \pm 20\ nm$ (we are leaving higher uncertainty because of the non-ideal shape of the structure gives a higher span of measured sizes).

A dedicated optical setup was developed for the controlled exposure of the samples (see

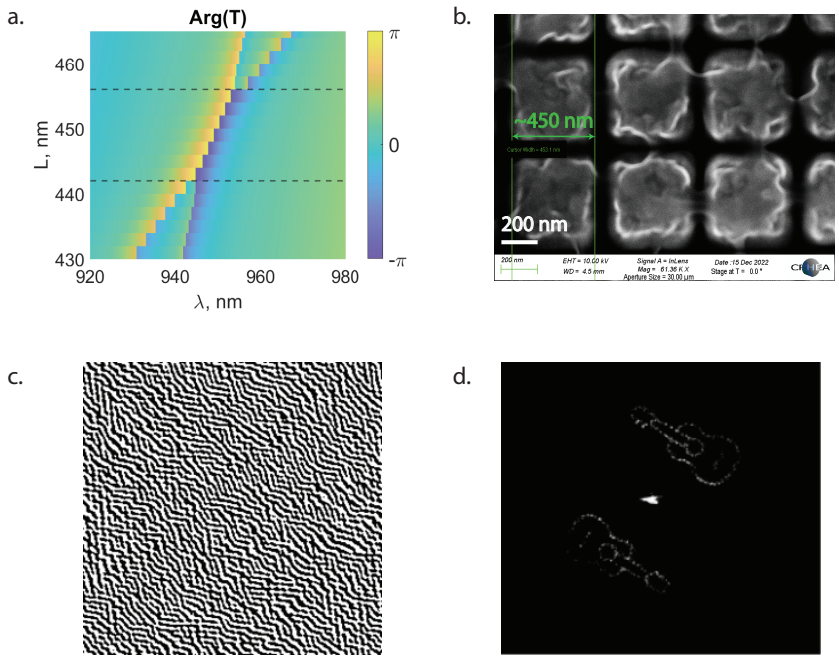

Figure 4: a. Transmission phase for the As_2S_3 Huygens metasurface operating around $\lambda = 940\ nm$ b. SEM-image of the fabricated up-scaled metasurface c. A binary phase pattern that was recorded on the metasurface by modulating the intensity of the exposure (at $\lambda = 532\ nm$) with SLM d. A hologram produced in a far field by the metasurface with a recorded phase pattern from (c.) upon illumination at $\lambda = 940\ nm$

the Methods section for its description). The intensity of green laser light illuminating the sample is varied using a spatial light modulator(SLM) producing only 2 levels of intensity. The produced intensity profile is then imaged onto the chalcogenide metasurface to fabricate a binary phase pattern. A collimated 940 nm laser diode is then used to illuminate the recorded metasurface. The transmitted beam is finally focused with a 100 mm focal length lens and a CCD camera placed in the focal plane is used to image the far field intensity. Figure 4c. shows the recorded phase pattern and figure 4d. - the associated measured far-field intensity producing a guitar-shaped profile confirming that the recorded amplitude pattern was converted into the same phase pattern.

The advantage of this approach is that uniform metasurfaces can be fabricated with such mass-production techniques as nanoimprint[51,52] while the functionality can be recorded a-posteriori using digital optics tools such as a spatial light modulator (SLM).[53] In addition,

the phase distribution recording system could be combined with an in-situ optical control, which allows real-time monitoring of the phase element manufacturing process.

Conclusion

Dielectric Huygens metasurface is one of the most efficient resonant metasurfaces being a promising candidate for wavefront shaping in integrated optical devices. We suggest a new production method for such metasurfaces based on photosensitive chalcogenide As_2S_3 material that experiences refractive index changes upon external exposure. In this work, we realize a proof-of-concept experiment by, first, fabricating uniform As_2S_3 metasurfaces with electron-beam lithography, and, second, demonstrating their fine-tuning induced by absorption of high energy photons (blue and green) experimentally. We characterize fabricated metasurfaces with transmission amplitude and phase measurements which demonstrate excellent correspondence to simulations. We also confirm the possibility of recording phase patterns on the uniform As_2S_3 metasurfaces by varying the exposure amplitude with a spatial light modulator. This method aligns well with the currently ongoing effort in technology for the fabrication of large-scale metasurfaces with reliable and reproducible structural parameters. The uniform structures could be fabricated with such techniques as nanoimprint that is better adapted for mass-production of large-size metasurfaces than electron-beam lithography currently used in laboratory experiments.

Methods

Numerical modeling

Metasurface surrounded from both sides with the infinite glass media (n=1.5) was modeled using the Frequency-domain solver of CST Studio Suite (r) which uses the finite elements method combined with special broadband frequency sweep techniques. We used a Unit cell

boundary condition that considers a periodic structure while ensuring phase-matching for waves at different incidences. As a result, we calculate a complex transmission coefficient allowing us to extract transmission amplitude and phase.

Complex-frequency simulations were performed using the Maxwell solver JCMsuite based on a higher-order finite element method.[54] It calculates the metasurface response for complex excitation frequencies from which we extract transmission amplitude and phase.

Nanofabrication

A thin (2 nm) MnO adhesion layer was deposited on a one-inch round glass substrate (B270) using plasma-assisted electron beam deposition (Bühler Syrus Pro machine). A 195 nm-thick layer of As_2S_3 was deposited on top of it using the same technique, ensuring a high-density high uniformity layer. The precise As_2S_3 thickness was monitored using in-situ direct optical monitoring (Bühler OMS 5000) at 700 nm. A thin 2 nm additional SiO_2 layer was deposited on top of the As_2S_3 layer using the same technology but unassisted, to protect the surface from oxidation.

Deposited films were nanostructured with electron-beam lithography and argon plasma etching according to the following steps. The surface was prepared by cleaning in acetone, isopropyl alcohol (IPA), deionized(DI) water and then exposed to O_2 plasma at 150° for 1 minute. The CSAR 62 positive photoresist (AR 6200.09 from Allresist) was spin-coated at 4000rpm and baked on a hotplate for 1 minute at 150°C. Then, conductive resist Electra 92 (Allresist) was spin-coated at @4000rpm and baked for 2 minutes at 90°C. Electron-beam lithography was performed using a Pioneer system (Raith) with the following parameters: ≈ 7.6 mm working distance, 20 kV voltage, 7.5 μm aperture, and ≈ 0.02 nA beam current, 6 nm step size, dose varied from 40 $\mu C/cm^2$ to 48 $\mu C/cm^2$. After the e-beam exposure, the sample was rinsed for 30 seconds in the DI water to remove the conductive resist, then developed for 45 seconds in AR 600-549 developer (Allresist) to remove the exposed parts of the CSAR resist and dipped for 30 seconds to IPA to stop the development. The developed

sample was post-baked for 2 minutes at 130°C and subjected to the inductively coupled argon plasma etching for 3 minutes (Plassys, radiofrequency power 400 Watt, process pressure 10^{-4} mTorr, argon flow 3.8 standard cubic centimeters per second). The remaining non-exposed CSAR resist was removed by rinsing the sample in acetone for 20 minutes using the ultrasonic bath. Finally, the sample was spin-coated at 1000rpm using a 4% solution of PMMA in ethyl lactate and baked for 5 minutes on a hotplate at 170°C.

Optical characterization

Transmittance measurements were performed using a custom setup detailed herein.[55] The system uses a double monochromator (Gemini-180 from HORIBA Jobin Yvon) to select a narrow spectral window from the white laser-driven light source (Energetiq). The source is imaged in the sample plane using a system of objectives and a diaphragm. The sample plane is then imaged in the plane of a CCD camera. The setup allows recording intensity images at each wavelength, transmittance coefficient is calculated using a reference measured separately.

We characterized the samples with a quantitative phase imaging technique called quadri-wave lateral shearing interferometry. This technique is based on the association of the 2-dimensional diffraction grating placed at a millimetric distance from the sensor of a camera. We implemented this QLSI camera on a microscope to acquire quantitative images of optical path differences that we further convert into phase images using the equation $\phi = \frac{2\pi OPD}{\lambda}$. For the illumination, we used a monochromator (Hypermonochromator, Mountain Photonics GmbH associated with an Energetiq EQ-99X laser-driven light source (LDLS), purchased from Opton Laser International, hyperchromator DG-600-300/1250) mounted in a Köhler configuration.

A dedicated optical setup was developed for the controlled exposure of the samples in order to produce the optical hologram (Fig. 5). A green TEM00 532 nm continuous wave laser with a power of 1 W was employed to expose the fabricated uniform metasurface.

First, the beam is expanded with 2-magnification using two achromatic lenses L1 and L2 to shine a π-shaper and generate a flat-top beam. A new set of lenses (L3 and L4) are then used to expand the beam and illuminate a spatial light modulator (SLM). The SLM, placed in between crossed polarizers, is used to produce an amplitude profile with a pixel size of $8.5\mu m$. The amplitude pattern generated on the SLM is then imaged using a two-lens system (L5 and L6) with $1/3.7\times$ magnification directly on the metasurface in order to produce an identical amplitude pattern with $2.3\mu m$ pixel size in the sample through refractive index change.

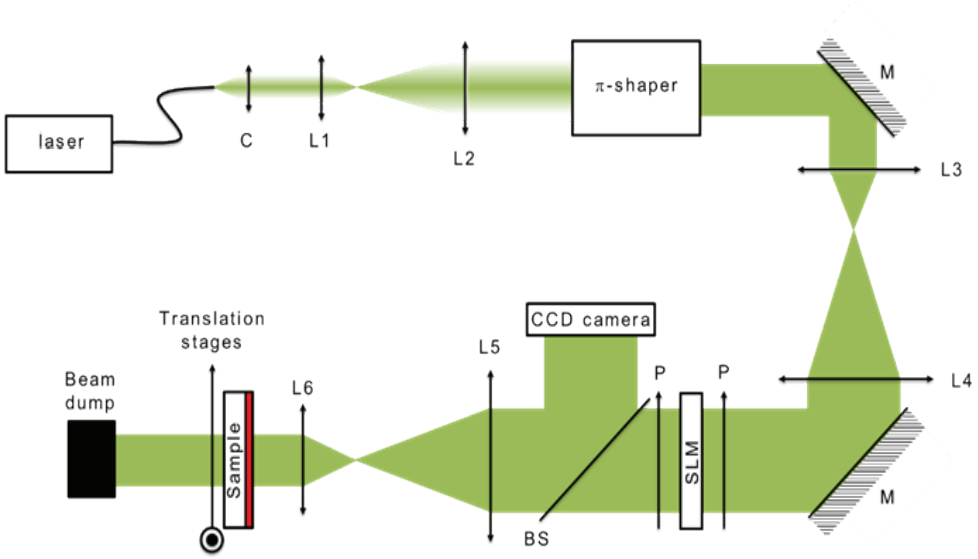

Figure 5: Setup dedicated to recording phase pattern by modulating the intensity of exposure with a spatial light modulator

Associated content

Supporting Information: complex frequency analysis of the As_2S_3 metasurface transmission in the vicinity of the exceptional point, numerical fit demonstrating square-root dependency of transmission zeros on the changing geometric parameter L in the vicinity of the exceptional point (PDF).

Acknowledgement

EM, RA, SE and JL acknowledge financial support from Multiwave Technologies SAS, the chalcogenide glass films were nanostructured at PLANETE nanofabrication platform (CT-PACA, member of the French Renatech+ network), PG and EM acknowledge financial support by the French National Research Agency ANR Project Meta-On-Demand (ANR-20-CE24-0013), RC acknowledges support from the European Innovation Council (EIC) project TwistedNano (under the grant agreement number Pathfinder Open 2021-101046424), RC, EM and PG acknowledge Dr. Sven Burger and JCMwave for their help and support with the JCMsuite software.

Supporting Information

Transmission zeros evolution in the vicinity of EP

Here, we show in more detail the transition from conventional operation regime (i) to Huygens regime (ii) and plot the complex plane calculation for three values of the parameter L highlighting this transition. Transmission amplitude ($Log_{10}(|T|)$) and phase ($Arg(T)$) were computed with JCMwave suite for $L = 370\ nm$, $L = 371.55\ nm$, and $L = 372\ nm$ (Fig. 6). Results in Fig. 6a.and c. correspond to the operation regime (i) and (ii) where two spectrally separated zeros of the first order, characterized by a phase vortex with a winding number 1, are observed[19]). Fig. 6 b. shows that for a certain parameter value ($L \approx 371.55\ nm$) the two zeros degenerate and merge together forming a zero of the second order, i.e. a transmissionless EP characterized by a winding number of 2 with a 4π phase accumulation encircling the singularity.

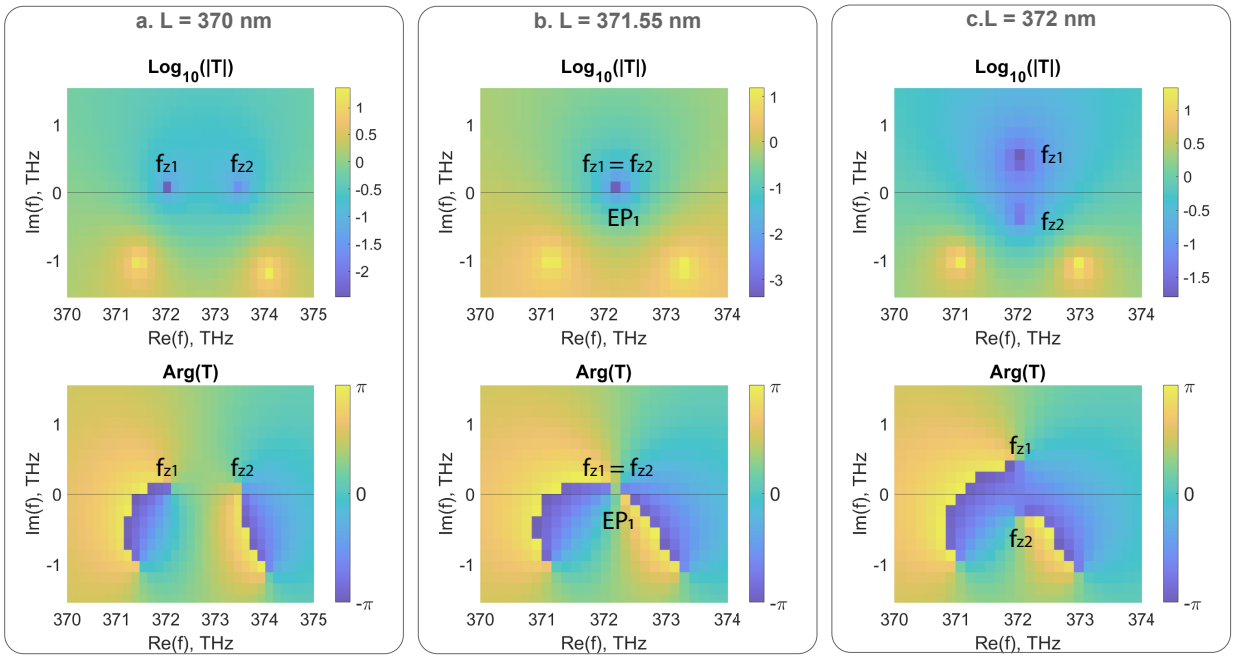

Figure 6: Transmission Amplitude and phase maps of an As_2S_3 metasurface excited with complex-frequency illumination impinging at normal incidence on metasurfaces designed with 3 specific values of the particles size L: a. For $L = 370\ nm$ the two zeros are spectrally separated and their eigenfrequencies are real-valued. b. For $L = 371.55\ nm$ the two complex zeros spectrally coincide forming transmissionless EP on the real axis. c. For $L = 372\ nm$ zeros have the same real part, but different imaginary parts, overall their complex eigenfrequencies being conjugated.

Fitting metasurface response to the parameter change in the vicinity of EP

The typical property of exceptional points in optical systems is the enhanced system's sensitivity to parameters change. This is because the system's response to this change depends non-linearly (as a square-root function) on the external change. We demonstrate this property for the considered structure by fitting the zeros trajectories in the vicinity of EP by the square root dependency on the size variation: $f = f_{EP_{1,2}} + \alpha_{1,2}\sqrt{L - L_{EP_{1,2}}}$. Fitted constant values are $\alpha_1 = -0.2045$ for the first zero and $\alpha_2 = 0.9896$ for the second zero. The comparison of the fitted curves with the numerically obtained transmission zero eigenfrequencies is shown in Fig. 7.

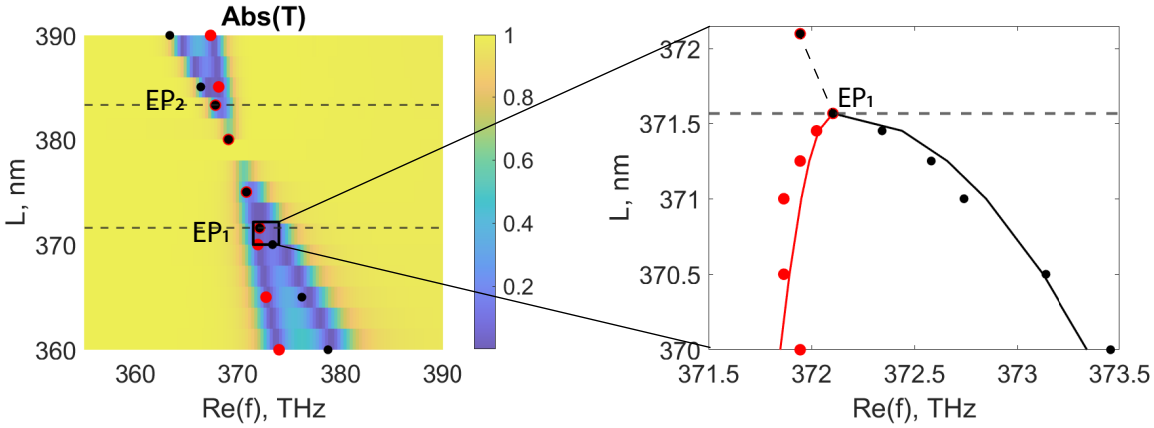

Figure 7: Metasurfaces's transmission spectrum amplitude with the selected area around the exceptional point is shown with a black rectangle. Zeros evolution in this area is shown in more detail in the figure on the right: numerical fit of zeros real parts trajectories in the vicinity of EP_1 indicates a typical square-root dependence of the system's response as a function of the small external parameter change (in this case, resonator's size). $f = f_{EP_1,2} + \alpha_{1,2}\sqrt{L - L_{EP_1,2}}$, are $\alpha_1 = -0.2045$ and $\alpha_2 = 0.9896$.

References

(1) Genevet, P.; Capasso, F.; Aieta, F.; Khorasaninejad, M.; Devlin, R. Recent advances in planar optics: from plasmonic to dielectric metasurfaces. *Optica* **2017**, *4*, 139.

(2) Chen, H.-T.; Taylor, A. J.; Yu, N. A review of metasurfaces: physics and applications. *Reports on Progress in Physics* **2016**, *79*, 076401.

(3) Scheuer, J. Optical Metasurfaces Are Coming of Age: Short- and Long-Term Opportunities for Commercial Applications. *ACS Photonics* **2020**,

(4) Mikheeva, E.; Kyrou, C.; Bentata, F.; Khadir, S.; Cueff, S.; Genevet, P. Space and Time Modulations of Light with Metasurfaces: Recent Progress and Future Prospects. *ACS Photonics* **2022**, acsphotonics.1c01833.

(5) Juliano Martins, R.; Marinov, E.; Youssef, M. A. B.; Kyrou, C.; Joubert, M.; Colmagro, C.; Gâté, V.; Turbil, C.; Coulon, P.-M.; Turover, D.; Khadir, S.; Giudici, M.;

Klitis, C.; Sorel, M.; Genevet, P. Metasurface-enhanced light detection and ranging technology. *Nature Communications* **2022**, *13*, 5724.

(6) Xie, Y.-Y.; Ni, P.-N.; Wang, Q.-H.; Kan, Q.; Briere, G.; Chen, P.-P.; Zhao, Z.-Z.; Delga, A.; Ren, H.-R.; Chen, H.-D.; Xu, C.; Genevet, P. Metasurface-integrated vertical cavity surface-emitting lasers for programmable directional lasing emissions. *Nature Nanotechnology* **2020**, *15*, 125–130.

(7) Astilean, S.; Lalanne, P.; Chavel, P.; Cambril, E.; Launois, H. High-efficiency subwavelength diffractive element patterned in a high-refractive-index material for 633??nm. *Optics Letters* **1998**, *23*, 552–554, Publisher: Optica Publishing Group.

(8) Lalanne, P. Waveguiding in blazed-binary diffractive elements. *JOSA A* **1999**, *16*, 2517–2520, Publisher: Optica Publishing Group.

(9) Khorasaninejad, M.; Aieta, F.; Kanhaiya, P.; Kats, M. A.; Genevet, P.; Rousso, D.; Capasso, F. Achromatic Metasurface Lens at Telecommunication Wavelengths. *Nano Letters* **2015**, *15*, 5358–5362.

(10) Wang, S. et al. A broadband achromatic metalens in the visible. *Nature Nanotechnology* **2018**, *13*, 227–232.

(11) Mikheeva, E.; Claude, J.-B.; Salomoni, M.; Wenger, J.; Lumeau, J.; Abdeddaim, R.; Ficorella, A.; Gola, A.; Paternoster, G.; Paganoni, M.; Auffray, E.; Lecoq, P.; Enoch, S. CMOS-compatible all-dielectric metalens for improving pixel photodetector arrays. *APL Photonics* **2020**, *5*, 116105.

(12) Bomzon, Z.; Biener, G.; Kleiner, V.; Hasman, E. Space-variant Pancharatnam–Berry phase optical elements with computer-generated subwavelength gratings. *Optics Letters* **2002**, *27*, 1141–1143.

(13) Khorasaninejad, M.; Crozier, K. B. Silicon nanofin grating as a miniature chirality-distinguishing beam-splitter. *Nature Communications* **2014**, *5*, 5386.

(14) Khorasaninejad, M.; Chen, W. T.; Devlin, R. C.; Oh, J.; Zhu, A. Y.; Capasso, F. Metalenses at visible wavelengths: Diffraction-limited focusing and subwavelength resolution imaging. *Science* **2016**, *352*, 1190–1194.

(15) Decker, M.; Staude, I.; Falkner, M.; Dominguez, J.; Neshev, D. N.; Brener, I.; Pertsch, T.; Kivshar, Y. S. High-Efficiency Dielectric Huygens' Surfaces. *Advanced Optical Materials* **2015**, *3*, 813–820.

(16) Yu, Y. F.; Zhu, A. Y.; Paniagua-Domínguez, R.; Fu, Y. H.; Luk'yanchuk, B.; Kuznetsov, A. I. High-transmission dielectric metasurface with 2π phase control at visible wavelengths: High-transmission dielectric metasurface with 2π phase control at visible wavelengths. *Laser & Photonics Reviews* **2015**, *9*, 412–418.

(17) Haim, D. B.; Michaeli, L.; Avayu, O.; Ellenbogen, T. Tuning the phase and amplitude response of plasmonic metasurface etalons. *Optics Express* **2020**, *28*, 17923.

(18) Park, J. et al. All-solid-state spatial light modulator with independent phase and amplitude control for three-dimensional LiDAR applications. *Nature Nanotechnology* **2021**, *16*, 69–76.

(19) Colom, R.; Mikheeva, E.; Achouri, K.; Zuniga-Perez, J.; Bonod, N.; Martin, O. J. F.; Burger, S.; Genevet, P. Crossing of the branch cut: the topological origin of a universal 2π-phase retardation in non-Hermitian metasurfaces. *arXiv:2202.05632 [physics]* **2022**,

(20) Cheng, J.; Ansari-Oghol-Beig, D.; Mosallaei, H. Wave manipulation with designer dielectric metasurfaces. *Optics Letters* **2014**, *39*, 6285.

(21) Wang, L.; Kruk, S.; Tang, H.; Li, T.; Kravchenko, I.; Neshev, D. N.; Kivshar, Y. S. Grayscale Transparent Metasurface Holograms. *Optica* **2016**, *3*, 1504.

(22) Chong, K. E.; Wang, L.; Staude, I.; James, A. R.; Dominguez, J.; Liu, S.; Subramania, G. S.; Decker, M.; Neshev, D. N.; Brener, I.; Kivshar, Y. S. Efficient Polarization-Insensitive Complex Wavefront Control Using Huygens' Metasurfaces Based on Dielectric Resonant Meta-Atoms. *ACS Photonics* **2016**, *3*, 514–519.

(23) Li, Q.-T.; Dong, F.; Wang, B.; Gan, F.; Chen, J.; Song, Z.; Xu, L.; Chu, W.; Xiao, Y.-F.; Gong, Q.; Li, Y. Polarization-independent and high-efficiency dielectric metasurfaces for visible light. *Optics Express* **2016**, *24*, 16309.

(24) Zhao, W.; Jiang, H.; Liu, B.; Song, J.; Jiang, Y.; Tang, C.; Li, J. Dielectric Huygens' Metasurface for High-Efficiency Hologram Operating in Transmission Mode. *Scientific Reports* **2016**, *6*, 30613.

(25) Shanei, M. M.; Hashemi, M.; Fathi, D.; Zapata-Rodríguez, C. J. Dielectric metalenses with engineered point spread function. *Applied Optics* **2017**, *56*, 8917.

(26) Zhou, Z.; Li, J.; Su, R.; Yao, B.; Fang, H.; Li, K.; Zhou, L.; Liu, J.; Stellinga, D.; Reardon, C. P.; Krauss, T. F.; Wang, X. Efficient Silicon Metasurfaces for Visible Light. *ACS Photonics* **2017**, *4*, 544–551.

(27) Bar-David, J.; Mazurski, N.; Levy, U. In Situ Planarization of Huygens Metasurfaces by Nanoscale Local Oxidation of Silicon. *ACS Photonics* **2017**, *4*, 2359–2366.

(28) Tian, J.; Yang, Y.; Qiu, M.; Laurell, F.; Pasiskevicius, V.; Jang, H. All-dielectric $KTiOPO_4$ metasurfaces based on multipolar resonances in the terahertz region. *Optics Express* **2017**, *25*, 24068.

(29) Liu, S.; Vaskin, A.; Campione, S.; Wolf, O.; Sinclair, M. B.; Reno, J.; Keeler, G. A.; Staude, I.; Brener, I. Huygens' Metasurfaces Enabled by Magnetic Dipole Resonance Tuning in Split Dielectric Nanoresonators. *Nano Letters* **2017**, *17*, 4297–4303.

(30) Ollanik, A. J.; Smith, J. A.; Belue, M. J.; Escarra, M. D. High-Efficiency All-Dielectric Huygens Metasurfaces from the Ultraviolet to the Infrared. *ACS Photonics* **2018**, *5*, 1351–1358.

(31) Yoon, G.; Lee, D.; Nam, K. T.; Rho, J. Pragmatic Metasurface Hologram at Visible Wavelength: The Balance between Diffraction Efficiency and Fabrication Compatibility. *ACS Photonics* **2018**, *5*, 1643–1647.

(32) Iyer, P. P.; Butakov, N. A.; Schuller, J. A. Reconfigurable Semiconductor Phased-Array Metasurfaces. *ACS Photonics* **2015**, *2*, 1077–1084.

(33) Komar, A.; Fang, Z.; Bohn, J.; Sautter, J.; Decker, M.; Miroshnichenko, A.; Pertsch, T.; Brener, I.; Kivshar, Y. S.; Staude, I.; Neshev, D. N. Electrically tunable all-dielectric optical metasurfaces based on liquid crystals. *Applied Physics Letters* **2017**, *110*, 071109.

(34) Li, S.-Q.; Xu, X.; Maruthiyodan Veetil, R.; Valuckas, V.; Paniagua-Domínguez, R.; Kuznetsov, A. I. Phase-only transmissive spatial light modulator based on tunable dielectric metasurface. *Science* **2019**, *364*, 1087–1090.

(35) Leitis, A.; Heß ler, A.; Wahl, S.; Wuttig, M.; Taubner, T.; Tittl, A.; Altug, H. All-Dielectric Programmable Huygens' Metasurfaces. *Advanced Functional Materials* **2020**, 1910259.

(36) Hisakuni, H.; Tanaka, K. Optical Fabrication of Microlenses in Chalcogenide Glasses. *Optics Letters* **1995**, *20*, 958.

(37) Hayashi, K.; Kato, D.; Shimakawa, K. Photoinduced Effects in Amorphous Chalcogenide Films by Vacuum Ultra-Violet Light. *Journal of Non-Crystalline Solids* **1996**, *198-200*, 696–699.

(38) Bourgade, A.; Lumeau, J. Large Aperture, Highly Uniform Narrow Bandpass

Fabry–Perot Filter Using Photosensitive As $_2$ S $_3$ Thin Films. *Optics Letters* **2019**, *44*, 351.

(39) Choi, D.-Y.; Wade, A.; Madden, S.; Wang, R.; Bulla, D.; Luther-Davies, B. Photo-Induced and Thermal Annealing of Chalcogenide Films for Waveguide Fabrication. *Physics Procedia* **2013**, *48*, 196–205.

(40) Hutley, M. C.; Maystre, D. The total absorption of light by a diffraction grating. *Optics Communications* **1976**, *19*, 431–436.

(41) Depine, R. A.; Brudny, V. L.; Simon, J. M. Phase behavior near total absorption by a metallic grating. *Optics Letters* **1987**, *12*, 143–145.

(42) Botten, L. C.; Cadilhac, M.; Derrick, G. H.; Maystre, D.; McPhedran, R. C.; Neviere, M.; Vincent, P. In *Electromagnetic Theory of Gratings*, softcover reprint of the original 1st ed. 1980 edition ed.; Petit, R., Ed.; Springer: Berlin, Heidelberg, 2011.

(43) Maystre, D. In *Plasmonics*; Enoch, S., Bonod, N., Eds.; Springer Berlin Heidelberg: Berlin, Heidelberg, 2012; Vol. 167; pp 39–83.

(44) Grigoriev, V.; Varault, S.; Boudarham, G.; Stout, B.; Wenger, J.; Bonod, N. Singular analysis of Fano resonances in plasmonic nanostructures. *Physical Review A* **2013**, *88*, 063805.

(45) Krasnok, A.; Baranov, D.; Li, H.; Miri, M.-A.; Monticone, F.; Alú, A. Anomalies in light scattering. *Advances in Optics and Photonics* **2019**, *11*, 892.

(46) Sweeney, W. R.; Hsu, C. W.; Stone, A. D. Theory of reflectionless scattering modes. *Physical Review A* **2020**, *102*, 063511.

(47) Kang, Y.; Genack, A. Z. Transmission zeros with topological symmetry in complex systems. *Physical Review B* **2021**, *103*, L100201.

(48) Khadir, S.; Andrén, D.; Verre, R.; Song, Q.; Monneret, S.; Genevet, P.; Käll, M.; Baffou, G. Metasurface Optical Characterization Using Quadriwave Lateral Shearing Interferometry. *ACS Photonics* **2021**, *8*, 603–613.

(49) Baffou, G. Quantitative phase microscopy using quadriwave lateral shearing interferometry (QLSI): principle, terminology, algorithm and grating shadow description. *Journal of Physics D: Applied Physics* **2021**, *54*, 294002.

(50) Mikheeva, E.; Abdeddaim, R.; Enoch, S.; Lumeau, J.; Voznyuk, I.; Antonakakis, T. Optical metasurfaces, and associated manufacturing methods and systems, US Patent 0146710. **May 12, 2022**,

(51) Solmaz, M.; Park, H.; Madsen, C. K.; Cheng, X. Patterning Chalcogenide Glass by Direct Resist-Free Thermal Nanoimprint. *Journal of Vacuum Science & Technology B: Microelectronics and Nanometer Structures* **2008**, *26*, 606.

(52) Wang, F.; Wang, Z.; Mao, D.; Chen, M.; Li, Q.; Kananen, T.; Fang, D.; Soman, A.; Hu, X.; Arnold, C. B.; Gu, T. Light Emission from Self-Assembled and Laser-Crystallized Chalcogenide Metasurface. *Advanced Optical Materials* **2020**, *8*, 1901236.

(53) Joërg, A.; Lumeau, J. Fabrication of Binary Volumetric Diffractive Optical Elements in Photosensitive Chalcogenide AMTIR-1 Layers. *Optics Letters* **2015**, *40*, 3233.

(54) Pomplun, J.; Burger, S.; Zschiedrich, L.; Schmidt, F. Adaptive finite element method for simulation of optical nano structures. *physica status solidi (b)* **2007**, *244*, 3419–3434.

(55) Lequime, M.; Abel-Tibérini, L.; Lumeau, J.; Gasc, K.; Berthon, J. Complex Pixelated Optical Filters. International Conference on Space Optics — ICSO 2014. Tenerife, Canary Islands, Spain, 2017; p 46.